Cryogenic Design of the EMCCD Cameras for the Brazilian Tunable Filter Imager

Denis Andrade,*[a,b], Dani Guzman[c], Olivier Daigle[d], Keith Taylor[b] , Claudia Mendes de Oliveira[b], Javier Ramirez Fernandez[a]
[a] Microelectronics Lab., POLI-USP, Sao Paulo University;
[b] Astronomy Department, IAG-USP, Sao Paulo University;
[c] AstroInventions Ltd., Chile;
[d] Univ. de Montréal, Canada;

ABSTRACT

In this paper we present the cryogenic design of the EMCCD (Electron Multiplication Charged Couple Device) cameras for the Brazilian Tunable Filter Imager instrument for the 4 meters SOAR telescope in Chile. The camera uses a E2V 1600 x 1600 pixels full-frame device, which is controlled by the new CCCP (CCD Controller for Counting Photons), an EMCCD controller developed by the University of Montreal. We present the design of the camera, its thermal analysis and cryogenic performance.

Keywords: EMCCD, cryogenic camera, astronomical instrumentation.

1. INTRODUCTION

The BTFI (Brazilian Tunable Filter Imager) is a new interferometric optical imager under development by a partnership of national (Brazilian) and international institutions. The BTFI will be mounted on the 4 meters SOAR telescope [1] in Chile. The new technology used in this equipment makes it extremely versatile: it introduces the iBTF (imaging Bragg Tunable Filter) concept [2] and a it will use two Fabry-Perots (FPs) [3]: one in the pupil plane acting as a high resolution imaging interferometer and the other in the uncollimated image space as a low-resolution tunable filter.

The instrument will also have two EMCCD (Electron Multiplication Charged Couple Device) cryogenic cameras, which allow for rapid scanning within the wavelength range of the instrument, for both the filtered light and a complementary channel that can be used as a simultaneous monitor of sky conditions [4].

The detectors will be readout by CCCP (CCD Controller for Counting Photons) [5]. This detector controller, developed at the Laboratory for Experimental Astrophysics in University of Montreal uses a new clocking architecture optimized for driving the EMCCDs at up to a 20MHz pixel rate and a fast vertical transfer. With this controller the Clock Induced Charge (CIC) noise, which is the dominant noise source in EMCCDs at low flux levels and high frame rates becomes very low (0.001 – 0.0018 electron/pixel/frame), over the range of the EM gain employed. These low noise levels make the EMCCD to behave as a near-perfect photon-counting device for very low fluxes [5].

* *denis@astro.iag.usp.br; phone: + 55 11 7332 3231; astro.iag.usp.br/~denis/*

2. THE EMCCD DETECTOR

BTFI is being developed for faint source observations. In order to achieve this goal, its detector has to work in a "rapid scanning" mode where the selected wavelength is continuously scanned. This means that a massive 3-dimensional data-cube will be acquired and integrated to achieve the required signal-to-noise. By using a "rapid scanning" technique, problems from atmospheric turbulence and variable extinction over long exposures will be eliminated by taking the average of all accumulated frames in the data-cube. Normal CCDs are non-optimal under these circumstances, as the readout noise will dominate the noise from the target's signal. To avoid this problem, EMCCD detectors are used. The main advantage of the EMCCD is that its readout noise is very low in the "photo counting" mode (or PMC).
EMCCD detectors are basically a normal CCD with an extended register responsible for an electron multiplication caused by the impact ionization on silicon. This phenomenon increases the detection performance since it amplifies the input interest signal. Performance gets improved, with an equivalent noise of less than 1 electron at high pixel rates [6].

Figure 1 shows a typical architecture of a frame transfer EMCCD. The image area – where photons are detected and collected – the store area and the readout register are of conventional CCD design. The "gain register" located between the output amplifier and the readout register is where the electron multiplication occurs [7]. In the case of our CCDs, a full-frame architecture is implemented, with no store area. This reduces the maximum sustained frame rate, but we can still achieve the frame rates required by the instrument.

The CIC noise is generated by the clocking transitions in the image and store areas of the detector as well as in the serial register. These transitions produce electrons that will be taken as real photons. CIC is the dominant source of noise in EMCCD detectors operating at high transfer rates [8,9].

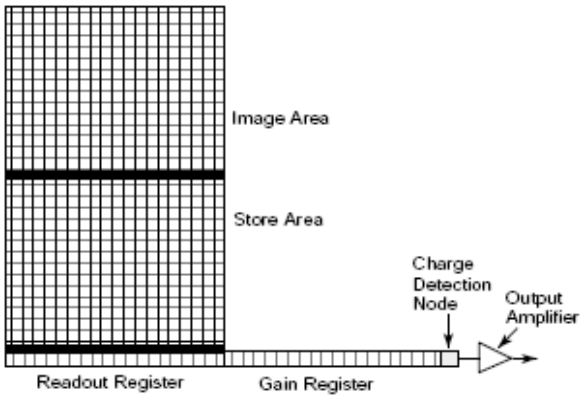

Figure1. Frame transfer EMCCD, with image and store areas indicated.

3. CAMERA DESIGN

The camera operates the EMCCD detector at cryogenic temperatures. It consists of a vacuum chamber, a cryogenic cooler, a detector "fan-out" board and electrical wiring to connect the detector to the exterior. The camera body is made of Aluminum., with a 50 mm BK7 window. There are two hermetic connectors for detector signals and temperature.

Internally the camera is composed by a cryogenic cooler coupled through a copper-made cold finger to the detector mount. The detector sits on a FR4 fan-out board. A radiation shield coupled to the cold finger completes the internal mechanics. Figure 2 shows some figures from the mechanical design of the camera and Figure 3 shows some pictures of the camera during the tests.

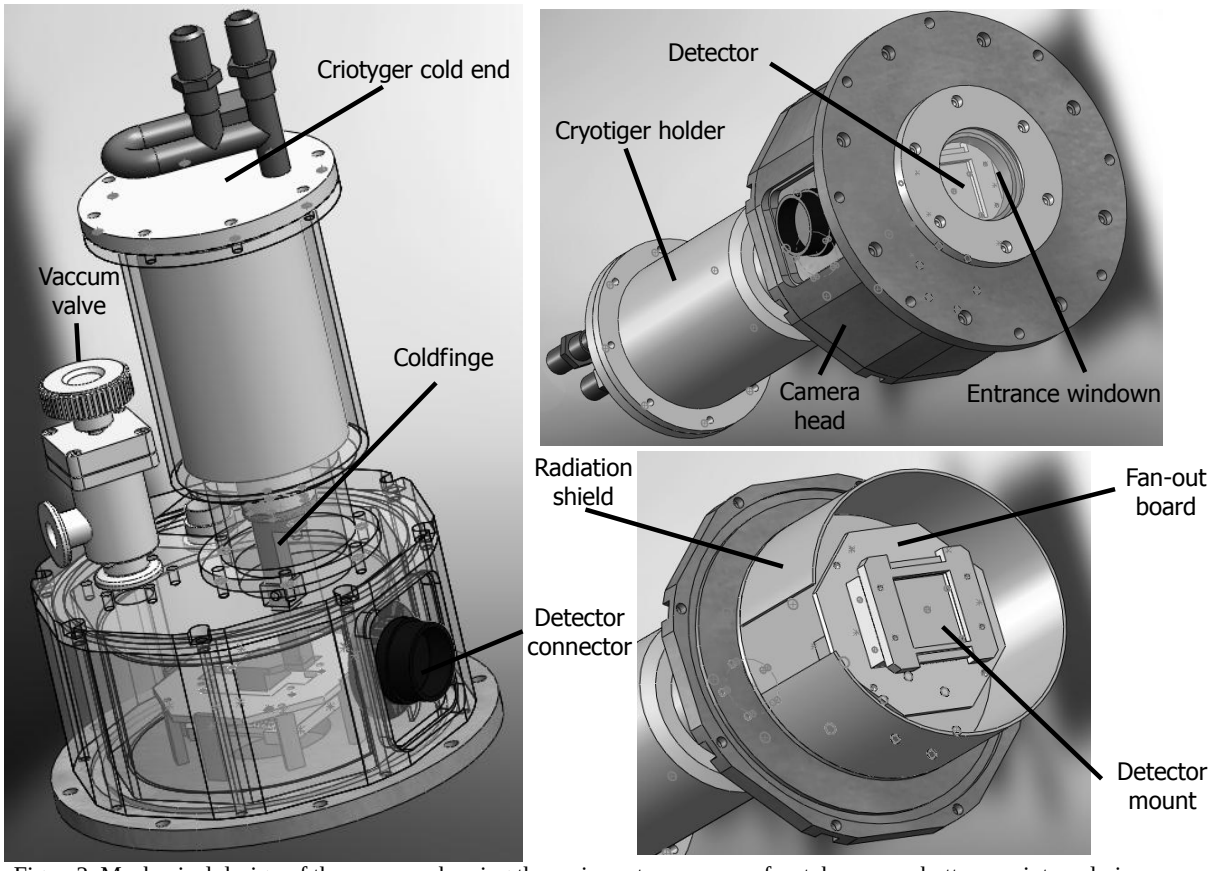

Figure2. Mechanical design of the camera, showing the main parts: a. camera front, b. camera bottom, c. internal view

Figure3. Pictures of the camera: a. camera front, b. internal view, c. camera top

4. THE COOLING SYSTEM AND THERMAL ANALYSIS

The cooling mechanism of the camera is a Cryotiger, a type of closed-cycle refrigerator that incorporates a compressor and a cold-end, linked by pressurized gas lines, using a proprietary gas blend based on propane. “Cryotiger” is its most common name in Astronomy, but the current version of this cryogenic cooler is called “PCC”, produced by a division of Brooks (www.brooks.com). PCC can be ordered with different gas blends, still using the same main components of compressor and cold-end. The type of gas used defines the cooling capacity and the minimum temperature the system can reach. SOAR runs a PCC in a different instrument already, so there is interest in using the same gas blend in BTFI’s cameras for maintainability. The existing PCC at SOAR uses gas PT-30, thus BTFI’s cameras use the same kind of gas and the analysis presented here assumes this gas.

The thermal analysis goal is to show that, using the PCC cooling system with a PT-30 gas type, the camera is able to cool down the detector to the proper operating temperature for the EMCCD detector, which is about -100°C to -110°C. Under vacuum, the detector temperature will be defined by the thermal equilibrium due to heat transfer by radiation and conduction. The equilibrium is reached when the heat flows coming in and out of the detector mount are balanced. The free-running temperature is investigated in the simulations, to obtain the thermal equilibrium for the mount.

There are four main temperature drivers inside the camera. As mentioned before, the cooling element decreases the detector temperature by conduction, from the detector mount through the cold finger. The other three drivers which increase the camera temperature are:

- The camera window: increase the temperature by radiation

- The camera body: increase the detector mount temperature by radiation. Its effect is minimized using the radiation shield

- The cabling: increase the detector mount temperature by conduction from the hermetic connectors through the cooper wires

Using the classic Stefan-Boltzmann Equation [12], the radiation, conduction and thermal joint conductance where analyzed. For the radiation conduction we have:

$$P_r = e\sigma A\left(T_r^4 - T_d^4\right) watt \quad (1)$$

Where:
e: emissivity of radiator
σ: Stefan-Boltzmann’s constant, 5.6703×10^{-8} watt/m^{2}K^4
A: Area of radiator
T_r: Temperature of the radiator
T_d: Temperature of the detector mount

And the conduction: heat transfer by conduction through an element where a temperature difference exists is given by [13]:

$$P_c = \frac{kA}{d}\left(T_{hot} - T_{cold}\right) watt \quad (2)$$

Where:
k: thermal conductivity of the element
A: cross section of the element
d: length of the element

The thermal joint conductance: the conductance of a interface – where two elements are touching each other and a certain pressure is applied to the joint – can be approximated with the following model [14]:

$$h = 1.25 k_s \frac{m}{\delta} \left(\frac{P}{H_c} \right)^{0.95} watt/K \quad (3)$$

Where:

$k_s = \frac{2 k_1 k_2}{k_1 + k_2}$ is the harmonic mean thermal conductivity of the interface; k_1 and k_2 are the conductivity of each element;

$\sigma = \sqrt{\sigma_1^2 + \sigma_2^2}$ is the effective RMS surface roughness of the contacting asperities;

$m = \sqrt{m_1^2 + m_2^2}$ is the effective mean absolute asperity slope of the interface.
It can be approximated as $m = 0.125(\sigma \times 10^6)^{0.402}$;

$P = \frac{F}{A}$ is pressure (Force / Area);

H_c is the surface microhardness of the softer of the two elements.

The only place where it is relevant to calculate the thermal conductance of an interface this way is between the cold finger and the detector mount, given this is the main interface by pure contact (not bolted) between two thermally conductive materials.

4.1 Radiation Shield

The radiation shield is attached to the cold finger; therefore its temperature depends on the cold finger, which in turn depends on the detector mount. The shield gets heat up by radiation from the camera body, producing a temperature gradient along its length, which is a function of the thermal conductance of the shield's material itself. The simulations implemented calculate the temperature profile of the shield and this is used to obtain the radiation coming from the shield to the detector. Radiation from the camera body is not included in the main thermal equilibrium then.

4.2 Thermal Equilibrium

The equilibrium is reached when the following equation is satisfied:

$PC_{finger} = PR_{window} + PR_{plate} + PRs_{hield} + PC_{cables}$ (7)

Where:
PC_{finger}: heat transfer by conduction between the mount and PCC, conducted by the cold finger and the interface joint between the mount and cold finger;
PR_{window}: heat transfer by radiation from the camera window;
PR_{plate}: heat transfer by radiation from the camera bottom plate (which does not have radiation shield);
PR_{shield}: heat transfer by radiation from the radiation shield, which is cooled by the cold finger;
PC_{cables}: heat transfer by conduction between the hermetic connector and the detector, conducted by the cables and PCB copper traces;

Finding the thermal equilibrium is an iterative process, since the heat transfer is calculated using the detector temperature, which is the main unknown one is pursuing. Therefore, an initial temperature is assumed and an iterative algorithm increments the temperature until the thermal equilibrium is reached within a specified error (0.01 K for the results presented here).

In fact, the thermal equilibrium is reached after a certain time, e.g. there is a time constant and the whole problem can be modeled by a differential equation. The simulation tools developed for this analysis do not take in consideration the time constant; therefore the thermal equilibrium is only static. For the simulated cooldown cycle presented in the next section,

the thermal equilibrium is static as well, finding the thermal equilibrium for any given PCC cold-end temperature.

5. RESULTS

5.1 Thermal Simulation Results

The parameters used in the simulations are presented in table 1. Geometric parameters (dimensions of elements) were obtained from the 3D model, but are not included here for simplicity.

Table 1. Thermal parameters for the simulation

Parameter	Value	Notes
Emissivity Window	1	considered a black body
Emissivity Al (e)	0.1	An emissivity of 0.05 is quoted for polished Al, but a conservative 0.1 is used. [15]
Conductivity Al (□)	180	
Roughness Al (σ)	4.25×10^{-6}	From [16]
Microhardness Al (H_c)	9.12×10^{8}	From [16]
Emissivity Cu	0.1	Similar to the Al case[15]
Conductivity Cu	380	
Roughness Cu	1.98×10^{-6}	From [16]
Cold finger force	5	Newtons, equivalent to 0.5 Kg
Cable wire diameter	0.51	mm^2, equivalent to AWG #24
PCB copper traces	15	mils, of 1 oz copper
Temperature PCC	-144	Celsius
Temperature Room	+25	Celsius

Using these parameters, the simulation obtains the values showed in Table 2.

Table 2: Thermal simulation results

Variable	Value	Units
Detector Temperature	-132.37	Celsius
Total heat transfer	1.87	Watt

From table 2, the free-running temperature of about -130 C is adequate for operation at -110 C. We may do some fine tuning at the cold finger to reduce this gap in temperature, so the temperature control requires less power.

Figure 4 shows a plot of the temperature along the radiation shield. The graphic origin is where the radiation shield is closer to the coldfinger (cold end). One can notice that the heat loss is very small (about 2°C) along the shield body.

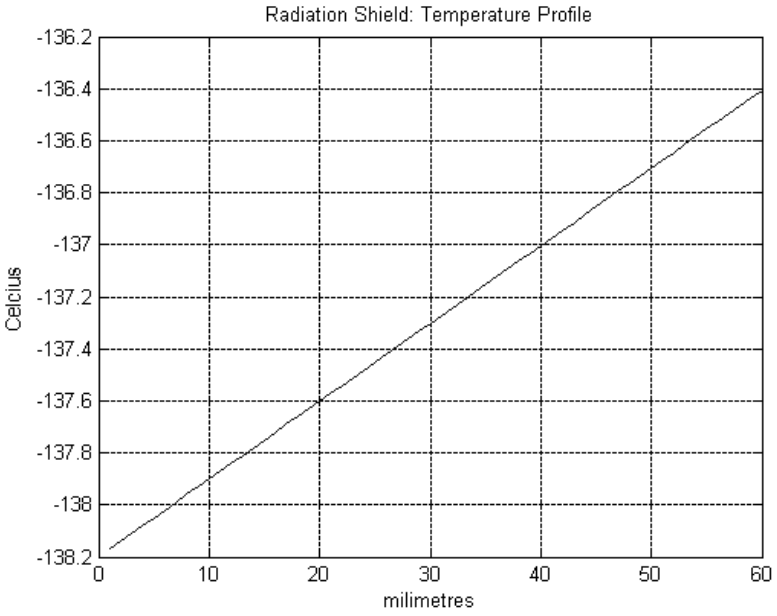

Figure 4. Radiation shield temperature along its length. Origin is closer to the cold finger

As next test, a cooldown is simulated, using a first-order exponential decay for the PCC temperature in time.

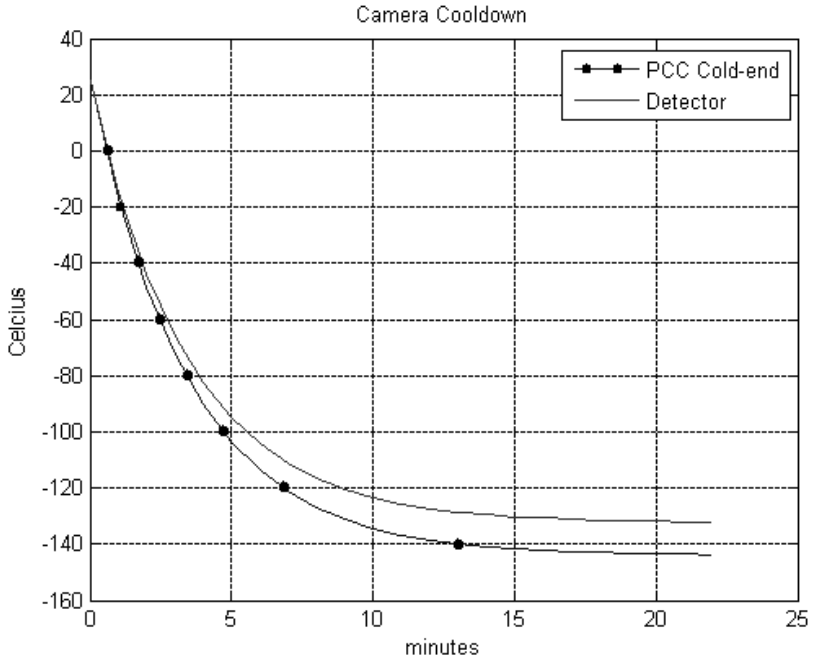

Figure 5: Simulation of a camera cooldown

It is important to note that the dynamic simulation in Figure 5 does not take into account the thermal inertia of the camera (a time constant), which is assumed to be zero for the simulation. Figure 5 only is only relevant to show the evolution of the two temperatures (PCC and detector) while cooling down. Experimental results with the camera will take longer to complete, as it will be seen in the next section.

5.2 Cameras thermal results

Here we show the detector temperature in the BTFI camera being cooled and controlled to be constant in -100°C. According to the detector supplier the maximum cooling rate recommended is of 5º per minute. One can note in Figure 6, that this value is never achieved. The curve maximum slope is about 2.3º per minute.

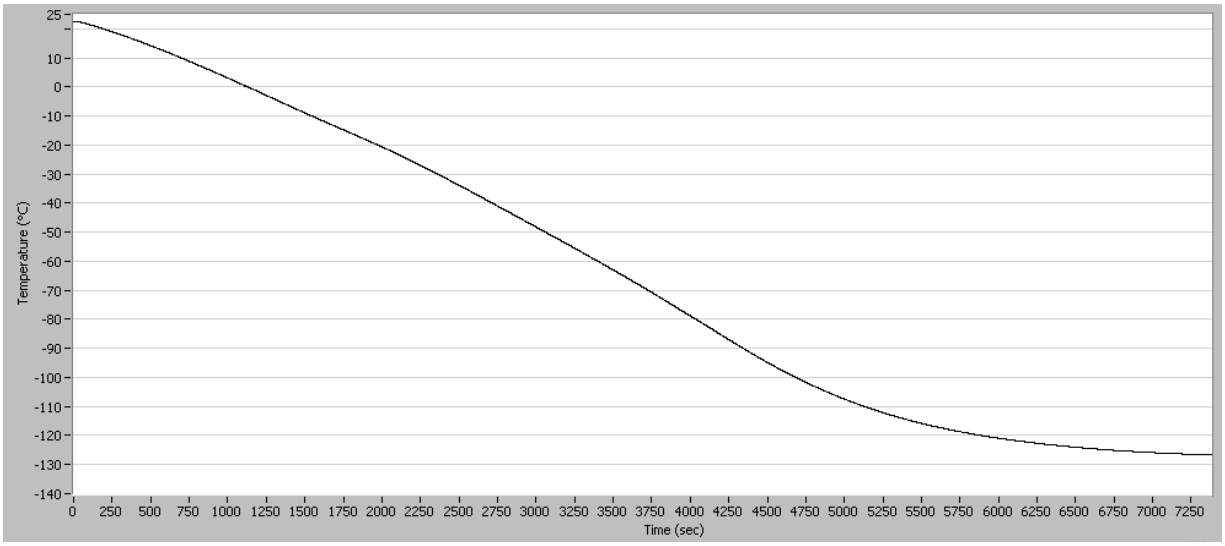

Figure 6. Real system cooldown from room temperature to -100ºC

Figure 7 shows the real system naturally coming back to room temperature with no external intervention. One can see in this image that it takes about 12 hours to the camera achieve room temperature again in these conditions.

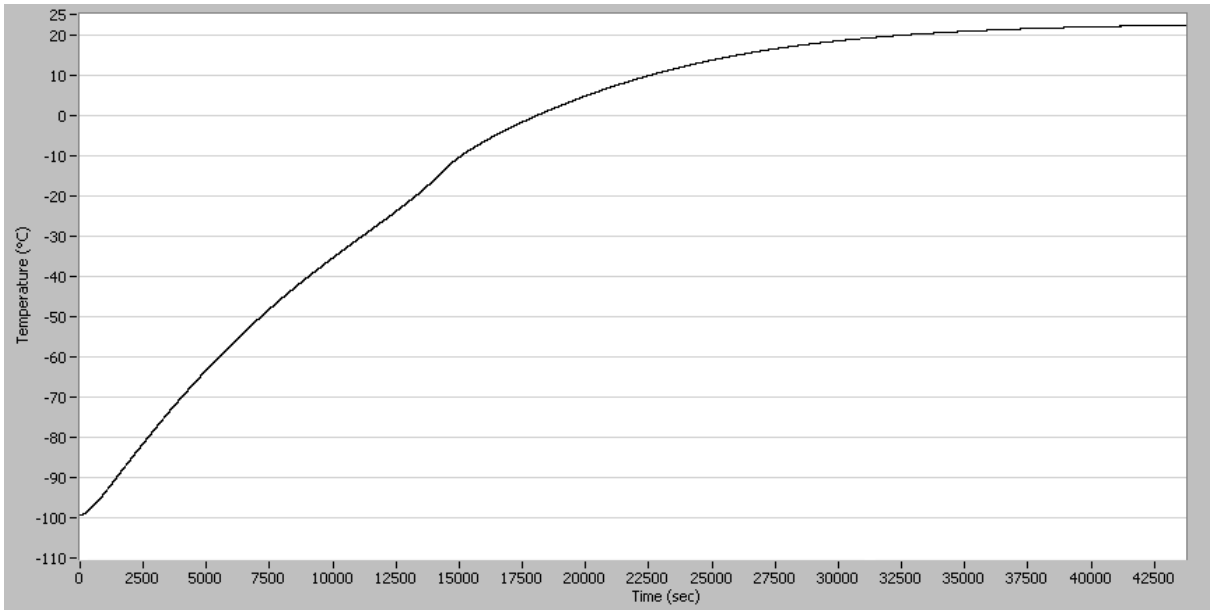

Figure 7. Real system coolup from -100ºC to room temperature

6. CONCLUSIONS

We have presented the thermal design, simulations and experimental results for the EMCCD cameras to be used with BTFI instrument. The camera accomplishes the requirements, regarding connections with the detector controller and free-running temperature .

The fan-out board, the connectors and cabling behaves adequately. During the laboratory tests we could measure that the signals are exactly the same if probed in the detector controller pins or in the detector socket. This means that the cabling is performing well and there is insignificant resistance and interference.

Cameras are currently undergoing intensive detector tests. We have one camera imaging in standard and EMCCD modes at 1 MHz, so we are concentrating in tuning CCCP for operation at 10MHz.

REFERENCES

[1] T.A. Sebring, G. Cecil and G. Moretto, “The SOAR telescope project: a four-metre telescope focussed on image quality”, Proc. SPIE, 3352 , 62–69, 1998.

[2] S. Blais-Ouellette, O. Daigle, K. Taylor, "The imaging Bragg tunable filter: a new path to integral field spectroscopy and narrow band imaging", Proceedings of the SPIE, Volume 6269, pp. 62695H, 2006.

[3] P. D. Atherton, "The Scanning Fabry-Perot Spectrometer” , 3D Spectral Methods in Astronomy, ASP Conference Series Vol. 71, 1995.

[4] B. Quint et al, “Illusion - A Fabry-Perot Data-Cube Synthesizer” - Astronomical Data Analysis Software and Systems XIX, ASP Conference Series, 2009, in press.

[5] O. Daigle, et al, “CCCP: A CCD Controller for Counting Photons”, SPIE, Vol. 7014, Jun, 2008.

[6] P. A. Jerram, P. J. Pool, D. J. Burt, R. T. Bell and M. S. Robbins, “Electron Multiplying CCDs” - SNIC Symposium, Stanford, California – 3-6 April 2006, e2v technologies ltd.

[7] P. Jerram, et al., “The LLLCCD: Low light imaging without the need for an intensifier” - Proceedings of SPIE, vol. 4306, p. 296, 2001.

[8] O. Daigle, et al, "Extreme faint flux imaging with an EMCCD" - Astronomical Society of the Pacific, 121:866–884, Aug. 2009.

[9] S. Tulloch, “Monte Carlo Modeling of L3 Detectors in High Time Resolution Applications,” in High Time Resolution Astrophysics: The Universe at Sub-Second Timescales , American Institute of Physics Conference Series 984 , pp. 148–161, Feb. 2008.

[10] S. Howell, “Handbook of CCD Astronomy” - Cambridge university press, first edition, United States of America, pp. 25-38, 1993.

[11] A. C. Moore, Z. Ninkov, W. J. Forrest, C. McMurtry, G. S. Burley, and L. Avery, “Operation and test of Hybridized Silicon p-i-n Arrays using Open-source Array Control Hardware and Software” - Proc. SPIE, 5017, pp. 240–253, Jan. 2003.

[12] http://hyperphysics.phy-astr.gsu.edu/hbase/thermo/stefan.html

[13] http://hyperphysics.phy-astr.gsu.edu/hbase/thermo/heatra.html

[14] M.M. Yovanovich, “New Contact and Gap Correlations for Conforming Rough Surfaces”, AIAA-81-1164, presented at AIAA 16th Thermophysics Conference, Palo Alto, CA., June 1981

[15] “Emissivity Values for Common Materials” - http://www.infrared-thermography.com/material.htm

[16] Yüncü, “Thermal contact conductance of nominally flat surfaces”, Heat Mass Transfer 43, I-5, 2006